

Crustal melting in orogenic belts revealed by eclogite thermal properties

Received: 22 December 2021

Accepted: 1 August 2022

Published online: 09 August 2022

 Check for updatesBaohua Zhang¹✉, Hongzhan Fei², Jianhua Ge^{3,4}, Lingsen Zeng⁵ & Qunke Xia¹✉

Partial melting in the continental crust may play a critical role on the behavior of continents during collision. However, the occurrence of partial melt in orogenic continental crust is not well understood. Since the temperature of the orogen is controlled by the thermal properties of constituent rocks, we measured the thermal conductivity and diffusivity of eclogite, the most important ultrahigh pressure metamorphic rocks, as a function of pressure, temperature, composition, and water content, and simulated the thermal structure of the Sulu and Himalaya-Tibet orogens in eastern and southwestern China, respectively. Our results show that the temperature at ~30-km depth beneath the orogens reaches the solidus of wet granite and phengite (~940 K), therefore, the partial melting in the orogenic continental crust is well explained. The melt may facilitate the exhumation of subducted crust, produce the low seismic-velocity zone, and cause the high-conductivity anomaly in the shallow depth of orogenic belts.

The most outstanding geophysical feature of the crust of orogenic belts is the presence of a widespread seismic low-velocity zone at depths of 20–50 km in global collision regions such as western Norway¹, Himalaya-Tibet in southwestern China^{2,3}, and Sulu in eastern China⁴. The seismic low-velocity zone is also frequently associated with high electrical conductivity values (up to 0.1 S/m), as interpreted by magnetotelluric (MT) observations^{5–9}. The origin of this low seismic velocity and high electrical conductivity remains highly debated. A few studies attributed these features to the hydration of eclogite¹⁰, which is composed of omphacite and garnet and is the main constituent rock of subduction zones and in the deep part of thickened continental crust^{1,3,11–13}. However, this hypothesis was later disproven by electrical conductivity experiments, which showed that hydrous eclogite cannot produce a conductivity value of 0.1 S/m¹⁴. Instead, partial melting can explain the observed geophysical anomalies in orogenic belts^{2,5–8} because the presence of melt can reduce the seismic velocity¹⁵ and enhance the electrical conductivity^{16–18}.

The question is why the orogenic continental crust can partially melt. As it is known, the melting of lithospheric rocks is controlled by the temperature distribution of the lithosphere, which is governed by heat flow from the deep mantle to the surface and thus controlled by the thermal properties of rocks and minerals, i.e., thermal diffusivity (D) and thermal conductivity (κ). A comprehensive understanding of the D and κ of eclogite under lowermost continental crust conditions is therefore necessary.

Nevertheless, the D and κ of eclogite under relevant high-pressure and high-temperature conditions of deep crust remain poorly constrained owing to experimental difficulties. A previous study reported D in a synthetic eclogite sample with a single component (MORB-composition) at 3.5 GPa¹⁹, and κ was calculated from D ²⁰ indirectly. However, the effects of pressure and modal mineralogy on the D and κ values of eclogite remain unknown, whereas such information is indispensable to infer the thermal structure of the continental lithosphere and thus to interpret the generation of

¹Key Laboratory of Geoscience Big Data and Deep Resource of Zhejiang Province, School of Earth Sciences, Zhejiang University, Hangzhou 310027, China.

²Bayerisches Geoinstitut, University of Bayreuth, Bayreuth D-95440, Germany. ³Advanced Batteries and Materials Engineering Research Center, Guizhou Light Industry Technical College, Guiyang 550025, China. ⁴Key Laboratory for High-Temperature and High-Pressure Study of the Earth's Interior, Institute of Geochemistry, Chinese Academy of Sciences, Guiyang 550081, China. ⁵Institute of Geology, Chinese Academy of Geological Sciences, Beijing 100037, China. ✉ e-mail: zhangbaohua@zju.edu.cn; qkxia@zju.edu.cn

partial melting and metamorphic and geochemical geodynamics of collisional orogen.

On the other hand, eclogites are formed through high-pressure to ultrahigh-pressure metamorphism. Regardless of the protoliths (e.g., gabbros or basaltic rocks), eclogites usually contain water in the constituted hydrous minerals (e.g., phengite, lawsonite, epidote) and nominally anhydrous minerals (e.g., omphacite, garnet). Upon with the increasing of temperature during continental deep subduction, the breakdown of hydrous minerals would leave omphacite and garnet as the main water reservoir in eclogite^{21–23}. Because water may affect the thermal properties of minerals^{24,25}, it is also necessary to investigate the water content dependence of D and κ .

In this study, multi-anvil experiments were performed to measure D and κ simultaneously in natural eclogite with various modal mineralogy and water contents at temperatures of 300–873 K and pressures of 1–3 GPa, corresponding to crust and lithospheric mantle conditions. Eclogite samples were collected from the Dabie-Sulu ultrahigh-pressure metamorphic (UHPM) belt in eastern China, which is the largest UHPM belt in the world. This belt is separated into western (Dabie UHPM belt) and eastern (Sulu UHPM belt) sections by the northeast-southwest trending Tan-Lu fault, thus two samples collected from representative outcrops in the Dabie UHPM belt (DB11 and DB13) and the other two samples from the Sulu UHPM belt (SL9 and SL12) were used (Supplementary Fig. 1).

Results and discussion

Temperature and pressure dependences of D and κ in eclogite

The D and κ values obtained under the investigated pressure and temperature conditions are listed in Supplementary Table 1. At 3 GPa, both D and κ are found to systematically decrease by a factor of 2–3 with increasing temperature from 300 to 873 K (Fig. 1a, b), and the temperature dependence decreases with increasing temperature. Despite the limited pressure range (1–3 GPa), Fig. 1c, d clearly show that both D and κ increases linearly with increasing pressure at given temperature conditions (300 and 823 K), whereas the pressure derivative ($\partial D/\partial P$ and $\partial \kappa/\partial P$) is steeper at 300 K than 823 K.

The measured D and κ for each sample were fitted by a power-law formulation²⁶ to simultaneously consider the influence of pressure and temperature on the thermal transport properties:

$$D = D_0 \left(\frac{300}{T} \right)^{n_D} (1 + aP) \quad (1)$$

$$\kappa = \kappa_0 \left(\frac{300}{T} \right)^{n_\kappa} (1 + bP) \quad (2)$$

where D_0 and κ_0 are the fitting results of D and κ under ambient conditions, respectively, P is pressure (GPa), T is temperature (K), n_D and n_κ are the temperature exponents, and a and b are the pressure

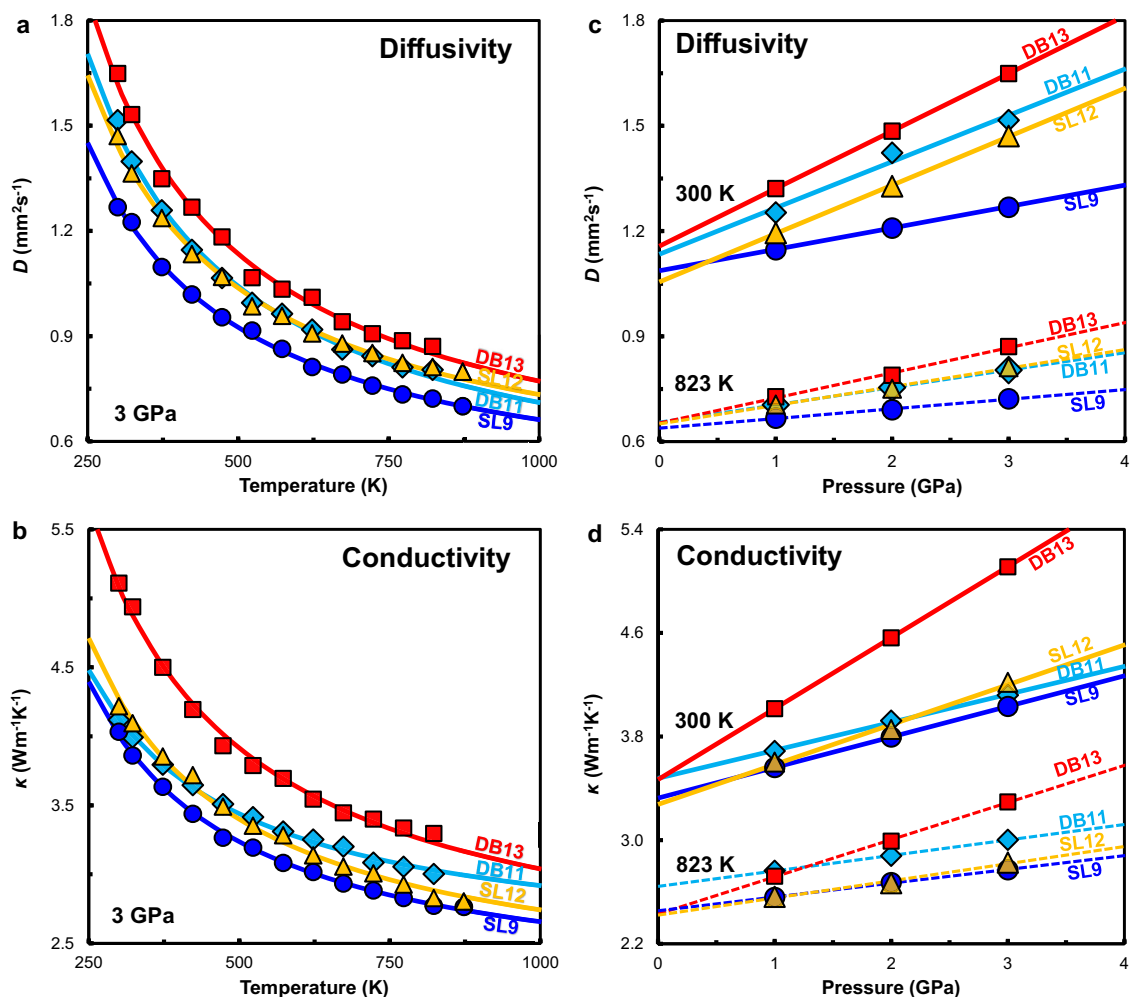


Fig. 1 | Temperature and pressure dependences of the thermal diffusivity (D) and conductivity (κ) of eclogite. a Temperature dependence of D at 3 GPa. **b** Temperature dependence of κ at 3 GPa. **c** Pressure dependence of D at 300 and

823 K. **d** Pressure dependence of κ at 300 and 823 K. The experimental error is less than 1.5% (Supplementary Table 1), and the error bars are smaller than the symbols.

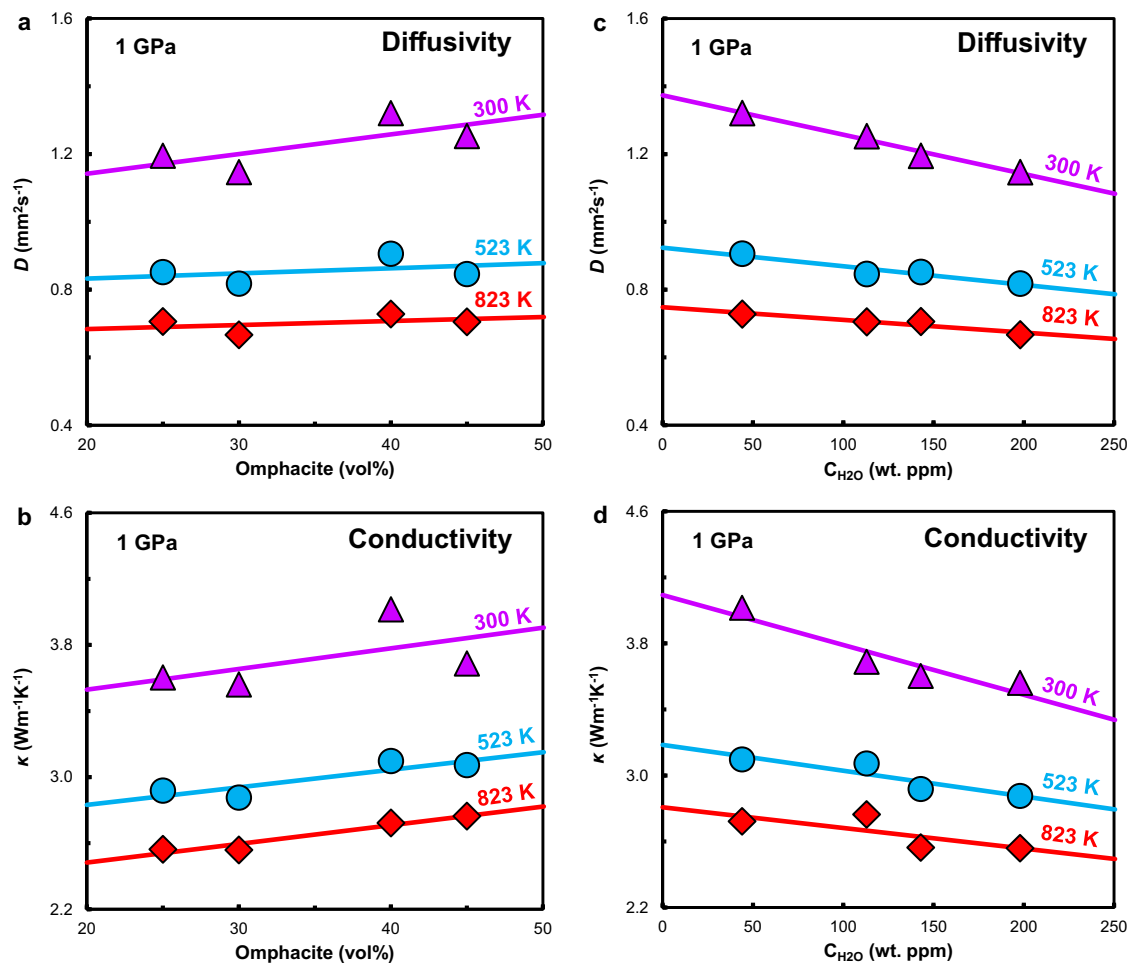


Fig. 2 | Effects of modal mineralogy and water content on the thermal properties of eclogite at 1 GPa and 300–823 K. a Effect of omphacite proportion on the thermal diffusivity (D). **b** Effect of omphacite proportion on the thermal

conductivity (κ). **c** Effect of water content on D . **d** Effect of water content on κ . The experimental error is less than 1.5% (Supplementary Table 1), and the error bars are smaller than the symbols.

coefficients. The least square fitting yields n_D , n_κ , a , and b values of 0.53–0.65, 0.31–0.49, 0.06–0.13 GPa⁻¹, and 0.06–0.24 GPa⁻¹, respectively (Supplementary Table 2).

Although the absolute values of D and κ in the four samples differ by ~30%, nearly identical temperature and pressure dependences were shown in this study. In terms of the heat transport mechanism, heat transfer in materials is known to be controlled by two subatomic processes: (1) the transfer of vibrational energy from one bond to another (i.e., phonon-phonon transport), which is inversely proportional to temperature and known as lattice thermal conductivity (κ_{lat}); and (2) the conversion of vibrational energy to light (i.e., phonon-photon conversion), which is proportional to the cube of temperature, and is known as radiative thermal conductivity (κ_{rad}). The κ_{lat} and κ_{rad} usually dominate at temperatures below and above 1000 K, respectively^{27,28}. The continuous decreasing of D and κ with increasing temperature up to 873 K in this study suggest that the thermal properties of eclogite is dominated by κ_{lat} . This is also confirmed by the theoretical calculation (Eq. 4): the calculated κ_{rad} is less than 3% of κ_{lat} at 300–873 K, namely, κ_{rad} has negligible effect to the experimental determination of κ_{lat} . On the other hand, the increase of D and κ with pressure is previously interpreted to be caused by the decrease of phonon scattering probability²⁹.

Influence of modal mineralogy and water

Mineral proportions may affect the D and κ of the bulk rock^{27,28} because different minerals have different thermal properties. In this study, the

eclogite samples were composed of 40–60 vol% garnet, 25–40 vol% omphacite, approximately 2 vol% quartz, and other minor phases including rutile, phengite, symplectite, apatite, epidote, amphibole, zoisite, and kyanite, with concentrations of less than 10 vol% each (Supplementary Fig. 2, Supplementary Table 3). The contributions of quartz and other minor phases should be negligible because of their small proportions even though quartz has higher D and κ than garnet and omphacite^{20,27,28,30}. Additionally, although the fraction of garnet is higher than that of omphacite, the D and κ of eclogite is found to be nearly independent of garnet content (Supplementary Fig. 3a, b) and slightly positively correlated with omphacite content (Fig. 2a, b). This is because the D and κ values of garnet are considerably lower than those of omphacite^{20,30}. Despite of the higher density and sound velocity of garnet than omphacite, specific heat capacity of omphacite is much larger than that of garnet, which would result in a larger mean free path for omphacite, namely, higher κ or D (Method section).

Although the thermal properties of eclogite have been determined experimentally^{19,20}, the effect of water on the D and κ of eclogites remains unknown. In this study, it is demonstrated that the D and κ of eclogite decrease linearly with increasing water content (Fig. 2c, d). Since thermal properties of eclogite are primarily controlled by omphacite as discussed above, water-content dependence of D and κ in eclogite should be controlled by the water-content in omphacite. In the viewpoint of mineral physics, water in eclogites mainly exists as hydroxyl in the crystal structures of garnet and omphacite^{10,14,31,32} (Supplementary Fig. 4). Hydroxyl could distort the crystal structures,

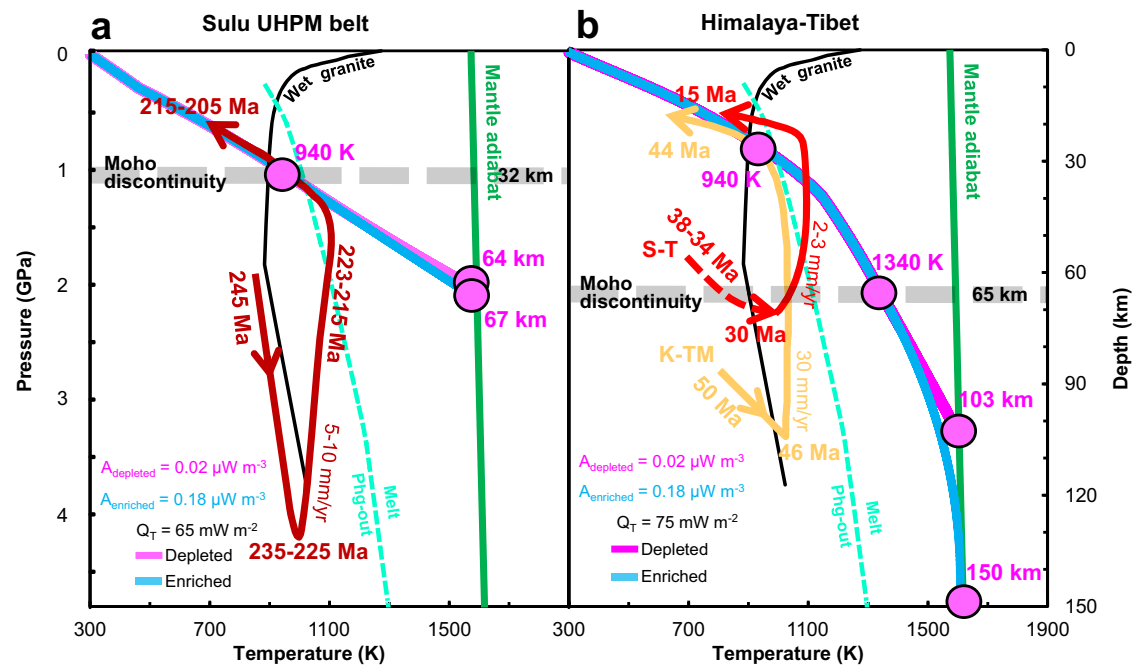


Fig. 3 | Geotherms of the crust and lithospheric mantle beneath orogenic belts.

a Sulu UHPM belt, **b** Himalaya-Tibet. The thick purple and light blue curves indicate the geotherm profiles calculated based on heat generation of $0.02 \mu\text{W m}^{-3}$ in the depleted mantle and $0.18 \mu\text{W m}^{-3}$ in the enriched mantle²¹, respectively. Solid black line: solidus of wet granite⁵⁴; thick light cyan dashed line: dehydration melting curve of phengite⁵³; thick green line: mantle adiabat line ($T_m = 1573 + 0.3z$ where z is

depth). The intersection between the calculated geotherm profile and mantle adiabat line indicates the thickness of the lithosphere, and the intersection between the geotherm profile and Moho discontinuity indicates the Moho temperature. P - T - t paths: The thick dark red line with arrows in **a** represents the Sulu UHPM belt^{21,58,60}. The thick red and orange lines with arrows in **b** represent the Southern Tibet (S-T)^{38,64} and Kaghan and Tso Morari (K-TM) terranes⁶³, respectively.

which produces additional phonon vibrational modes arising from new O-H bonds^{24,25,33} and thus enhancing the frequency of scattering events. It sequentially reduces the number of free paths for phonons and accordingly reduces D and k ^{24,25}.

Thermal structure and partial melting of orogenic belts

Numerous studies have provided petrological evidences for the occurrence of partial melting in natural UHP rocks during the continental collision^{34–40}. However, the temperature distribution beneath continental orogenic belts, which is essential for interpretation of the partial melt process during continental collision, is poorly understood. Based on the κ of eclogite under lithospheric pressure, temperature, and water-content conditions determined in this study and that of other rocks and minerals (olivine, granite, gneiss, amphibolite, and granulite) from literatures^{25,28,41,42}, numerical thermophysical modeling was performed to calculate the geotherms in the lithosphere of the Sulu orogenic belt (normal crust thickness, ~32 km) in eastern China and the Himalaya-Tibet orogenic belt (thickened crust, ~65 km) in southwestern China as two typical examples. The crustal structures, composition, and heat production of each belt was given in Supplementary Fig. 5. The water content in the continental mantle lithosphere was assumed to be constant ~100 wt. ppm⁴³. The surface heat flow (Q_T) was estimated to be 65 mW m^{-2} for the Sulu belt and 75 mW m^{-2} for the Himalaya-Tibet belt based on the database of surface heat flow^{44,45}. The mantle adiabat was set to a potential temperature of 1573 K with a gradient of 0.3 K/km, and the surface temperature was fixed at 283 K. A one-dimensional model with a boot-strapping approach (Eqs. 8–10)^{46,47} was used. Details of the calculation is given in the Methods section.

Figure 3 shows the modeled results of the temperature-depth profiles and average lithospheric thickness of the Sulu and Himalaya-Tibet belts. In the Sulu orogenic belt, the Moho temperature at depth of 32 km is ~940 K, and the inferred lithospheric thickness is around 64–67 km (Fig. 3a). In the Himalaya-Tibet orogenic belt, due to the differences in heat flow and heat production (Supplementary Fig. 5),

the temperature at Moho discontinuity (~65 km)^{48,49} reaches to 1340 K, and the lithospheric thickness is close to 150 km (Fig. 3b). The effect of radiogenic heat production (depleted versus enriched)^{50–52} on the lithospheric thickness is large in the Himalaya-Tibet orogen but negligible in the Sulu orogenic belt. Note that, although the crustal structure, composition, heat flow, and radiogenic heat production in the Sulu belt differ from those in the Himalaya-Tibet belt (Supplementary Fig. 5), the temperature (~940 K) at ~30 km depth of Sulu (base of the crust, close to Moho discontinuity of Sulu belt) is almost identical to that of Himalaya-Tibet belt at the same depth (middle crust of Himalaya-Tibet belt), and close to the solidus of phengite⁵³ and wet granite⁵⁴ (Fig. 3). Therefore, the shallowest regions for the occurrence of partial melt beneath the Sulu and Himalaya-Tibet belts are ~30 km depth, i.e., at base of crust near the Moho discontinuity and the middle crust, respectively. Namely, crustal melting in orogenic belts could occur beneath both the Sulu and the Himalaya-Tibet belts.

In addition to the Sulu and the Himalaya-Tibet belts, the other UHP belts worldwide, such as the Kokchetav massif (Kazakhstan), the Bohemia massif (Central Europe) and the Greenland, the temperature at ~30 km depth could reach the dehydration temperature of hydrous rocks as well^{21,22,55}. Water released by the dehydration depresses the melting point of rocks considerably, leading to partial melting in the deeper and hotter regions^{21,22,56} (Fig. 3).

Here the questions about when and why partial melting have occurred in the continental crust of the Sulu and the Himalaya-Tibet belts during their subduction and exhumation are discussed in detail. According to the SHRIMP U-Pb analysis of zircon^{57–60}, there are three important stages of pressure-temperature-time (P - T - t) paths for the metamorphic history of the Dabie-Sulu UHP rocks (Red curves in Fig. 3a), i.e., (1) 246–244 Ma for early-stage quartz eclogite-facies prograde metamorphism at 843–963 K and 1.7–2.1 GPa; (2) 235–225 Ma for peak UHP metamorphism at 1023–1123 K and 3.0–4.3 GPa; (3) 215–205 Ma for late-stage amphibolite-facies retrogression at 823–923 K and 0.7–1.0 GPa. The first episode of partial melting of Sulu

belt should occur at the beginning of the early stage of exhumation because the temperature of the exhumation rocks reaches the solidus of wet granite at ~120 km depth (3.8 GPa, 1050 K) (Fig. 3a), indicated by the occurrence of nanogranites in zircon, garnet and monazite from diatexite⁴⁰. Upon the decompression of “hot” exhumation, the breakdown of phengite could provide sufficient amount of the water and inducing the second episode of partial melting at ~60 km depth (2.0 GPa, 1095 K)^{11,21,39,40,57–62}, which was recorded by the presence of multiphase solid inclusions within UHP minerals and anatectic zircons and minor interstitial K-feldspar between garnet and omphacite in the Sulu UHP eclogites^{37,39,40}.

The Himalaya-Tibet belt has two types of eclogite with different P-T-t paths for subduction and exhumation processes^{38,63,64}: (1) ~50 Ma UHP eclogites in the Kaghan and Tso Moriri massifs in the western Himalaya (K-TM curve in Fig. 3b); (2) ~30 Ma HP eclogites distributed from central Himalaya to Southern Tibet (S-T curve in Fig. 3b). As illustrated in Fig. 3b, K-TM UHP slices has undergone one episode of partial melting at ~100 km depth (3.2 GPa, 1025 K) due to melting of fertile components at the initial stage of exhumation, whereas fluid-absent melting of phengite may continuously occur during the fast exhumation of felsic UHP rocks⁶². In contrast, the S-T UHP slice have undergone the first episode at ~70 km depth (2.1 GPa, 900 K, near Moho discontinuity of Himalaya-Tibet belt) due to the melting of fertile components and the second episode of partial melting at ~55 km depth (1.6 GPa, 1080 K) due to the melting of phengite.

The partial melt plays important roles in geodynamic and geophysical processes. For example, when partial melting takes place at the peak UHP metamorphic stage or at the final stage of subduction, the melts can reduce the strength the rocks, leading to the weakening of the deeply subducted continental crust and the decoupling of rocks from the subducting slab, which may result in the initiation of exhumation^{65–67}. When partial melting takes place during exhumation (generally caused by the breakdown of hydrous UHP minerals and the exsolution of water in NAMs), the melt channel may lubricate the edge of exhumated slices of UHP rocks and thus enhance the transport of materials from deep regions to the surface^{11,21–23,39,67}.

The onset of partial melting during subduction and exhumation of continental crust should also cause geophysical anomalies because partial melt could lower the seismic velocity and enhance the electrical conductivity of rocks^{15–18}. Therefore, the occurrence of partial melting in the lithosphere could explain the low seismic-velocity and high electrical conductivity observed in the lithosphere of Sulu^{4,8} and Himalaya-Tibet belts^{2,3,5–7,9}, which can hardly be explained by the hydration of eclogite in previous models based on water-enhanced electrical conductivity of omphacite¹⁴ unless an unrealistically high water capacity is assumed (0.7 wt.% H₂O).

Methods

Geological background and sample preparation

The Dabie–Sulu orogenic belt was formed by the Triassic subduction of the Yangtze craton beneath the Sino-Korean lithospheric plate^{58,68–70}. The Dabie–Sulu orogen is separated into two terranes by approximately 500 km of left-lateral strike-slip displacement along the Tan–Lu fault (Supplementary Fig. 1). The Dabie terrane in the west is the major segment bounded by the Tan–Lu fault and separated into a series of continuous zones by several large-scale EW-trending faults. The Sulu terrane in the east is segmented into a number of blocks by several NE–SW trending faults subparallel to the Tan–Lu fault. The Dabie–Sulu HP–UHP belts are unconformably overlain by Jurassic clastic sedimentary rocks and Cretaceous volcanoclastic deposits, and are intruded by post-collisional Mesozoic granites⁵⁹. The continental crust subducted to the mantle at 80–200 km depths as indicated by the coesite and diamond samples in the Dabie–Sulu UHP metamorphic belts, followed by large-scale UHP metamorphism and subsequent exhumation to the shallow crust demonstrated by the coesite and

microdiamond inclusions within zircon from gneisses^{58,69,70}. The eclogites in the Dabie–Sulu UHP terrane can be divided into three types based on their occurrence and host rocks. They are, Type I as enclaves or layers in granitic orthogneisses, Type II as enclaves in or interlayered with marbles, and Type III as enclaves and interlayers with ultramafic rocks^{58,71}. Geochronological studies^{59,69,72} indicated that the protolith ages of eclogites are 657–757 Ma for the Dabie belt and 747–788 Ma for Sulu belt, whereas metamorphic ages and exhumation ages are 225–235 Ma and ~230 Ma, respectively (Supplementary Table 3).

Four eclogite rock samples were used in this study: two (DB11 and DB13) collected from outcrops in Bixiling area, which is in the Central Dabie UHPM belt, and two (SL9 and SL12) collected from outcrops in Zhucheng and Rongcheng regions, both of which are in the northern part of the Sulu UHPM belt (Supplementary Fig. 1). These four samples were also used in previous study⁷¹. The mineral assemblage and major elements were reanalyzed in this study. All of the samples were fresh, fine-grained, and free of strong retrograde alteration. The concentrations of amphibole, epidote, biotite, aegirine, which are caused by garnet → biotite + epidote, and omphacite → amphibole + albite, are still very low (<4%) (Supplementary Table 3). Disks with a 6.0-mm diameter and 1.5-mm thickness were cored from the raw rocks, polished with sandpaper and 1-μm diamond powder, and dried in a vacuum oven at 473 K for 24 h before assembly.

Mineral assemblage analysis

The modal mineral abundances in each sample were determined by point counting under a polarizing microscope on a series of thin sections. The primary mineralogy of these samples is garnet (40–60 vol%), omphacite (25–40 vol%), symplectite (10–20 vol%), and small amounts of accessory minerals (rutile, quartz, apatite, phengite, epidote, zoisite, and kyanite). Detailed petrographic features of these four samples are shown in Supplementary Fig. 2, and the peak metamorphic temperatures and pressures are listed in Supplementary Table 3.

Major elements analysis

The chemical composition of each sample was determined by X-ray fluorescence spectrometry (Supplementary Table 4). The eclogitic rocks of Dabie and Sulu terranes showed a small variation in chemical composition. In a TAS (total alkali vs. silica) diagram (Supplementary Fig. 6), all of them fall in the category of picro-basalt and basalt. Geochemical studies indicated that the protoliths of Type I eclogites are basalts and that of Type III eclogites are continental gabbros^{58,71}. Water in fresh gabbros and basalts store in the phenocrysts (feldspar, pyroxene, etc.) and glasses, and the alteration minerals (amphibole, chlorite, etc.) formed by the water-rock interaction when exposed at the surface. The compositions of the garnet and omphacite phases were analyzed using an electron microprobe, which verified that both are chemically homogeneous. The concentrations of the major components in garnet and omphacite are summarized in Supplementary Table 5.

Infrared spectroscopy measurements

The water contents in the samples before and after the thermal property measurements were analyzed by Fourier-transformation infrared (FT-IR) spectroscopy using a Jasco FTIR-6200 Equipper with an IRT-7000 infrared microscope. The aperture size was 50 × 50 μm, which is sufficiently large to incorporate dozens of grains. More than five spots were measured on each constituent mineral using unpolarized light. Measurements were performed through optically clean, inclusion- and crack-free areas at 1 atm and 300 K with a continuous dry N₂ gas flow.

The water content in each mineral was calculated using the Beer–Lambert law $C_{\text{H}_2\text{O}} = \Delta / (I \times t \times \gamma)^{73}$, where $C_{\text{H}_2\text{O}}$ is the content of hydrogen species (wt. ppm H₂O), Δ is the integrated area of the -OH absorption bands (cm⁻²), I is the integral specific absorption coefficient

($\text{ppm}^{-1} \text{cm}^{-2}$), t is the thickness (cm, double-side polished to 0.12 cm prior to FT-IR analysis), and γ is the orientation factor discussed by Paterson⁷⁴. The -OH absorption bands were integrated between 2800 and 3800 cm^{-1} for garnet and between 3000 and 3800 cm^{-1} for omphacite to obtain the Δ values. Integral specific absorption coefficients of 1.39 and 7.09 $\text{ppm}^{-1} \text{cm}^{-2}$ were used for garnet and omphacite, respectively⁷³. An orientation factor γ of 1 was applied for garnet and 1/3 for omphacite⁷⁴. The bulk water content in eclogite (Supplementary Table 6) was estimated from the volume fraction and water content of each constituent mineral. The samples showed nearly identical FT-IR spectra before and after the thermal property measurements (Supplementary Fig. 4), thus indicating no water loss during the experiments. However, the general uncertainty of FTIR analysis is 30–50% caused by a number of reasons including unpolarized infrared on unoriented minerals, baseline correction, sample thickness uncertainty, and so on. The variation of water content in this study is indeed within the analytical uncertainty.

Thermal property measurements

Theory of experimental thermal property measurements. Heat transport in solids could occur by the vibration of atoms in the lattices and through the grain-boundaries. The vibrations of atoms about their equilibrium positions (crystal lattice) are strongly coupled with neighboring atoms. The vibrational energy is thus dissipated through excitation of adjacent atoms. A realistic model accounting for the quantization of the vibrations is referred to as phonons. Heat is thus transferred through collision of phonons with each other. With either increasing pressure or decreasing temperature, the vibration frequency will increase, leading to the increase of phonon collision frequency. As a result, the thermal conductivity increases.

In the Debye's model, the contribution of phonon scattering to thermal conductivity (κ_{lat}) is approximately expressed by the relation^{29,75}:

$$\kappa_{\text{lat}} = \frac{1}{3} C_V \nu \rho l \quad (3)$$

where C_V is the volume specific heat capacity, ν is average phonon velocity (approximately equal to the sound velocity of solids), ρ is the density, and l is the mean free path. The mean free path is an important parameter to evaluate the ability of heat transfer. For example, if the density, specific heat capacity, and sound velocity reported in garnet^{30,76} and omphacite^{20,77} are considered in Eq. (3), the mean free path (l) is estimated to be about 5.5 Å and 7.6 Å for garnet and omphacite, respectively, at 1 atm and 300 K. Even through the temperature rises to 800 K, the l value of omphacite (-3.5 Å) is still greater than that of garnet (-2.6 Å). A larger mean free path implies a higher κ or D , which may reflect the influence of crystal structure on heat transport properties.

In addition to transport by phonons, heat could be transport by thermal radiation through a transparent and little-absorbing medium as electromagnetic waves (photons). The radiative heat transfer (κ_{rad}) depends on temperature, frequency of the electromagnetic waves, and three different length parameters (i.e., the size of the particulates involved in physical scattering, the distance over which about half of the photon flux is absorbed, and the distance over which temperature changes significantly)⁷⁸. According to the blackbody radiation theory, κ_{rad} increases with the cube of temperature^{75,78}. At ambient pressure, κ_{rad} of ferrous minerals approximately follow the equation⁷⁵:

$$\kappa_{\text{rad}} = 8.57^3 / 10^{11} [\text{W}/(\text{mK})] \quad (4)$$

Therefore, the total thermal conductivity (effective thermal conductivity, κ_{eff}) of a solid can be written as

$$\kappa_{\text{eff}} = \kappa_{\text{lat}} + \kappa_{\text{rad}} \quad (5)$$

Generally, because of negative and positive temperature dependences of κ_{lat} and κ_{rad} , respectively, κ_{eff} is dominated by κ_{lat} at relatively low temperature conditions (<1000 K, corresponding to lithospheric temperature conditions), and by κ_{rad} at higher temperatures.

High-pressure experiments accompanied with thermal property measurements. The D and κ of the samples were measured on a DIA-type multi-anvil apparatus using a cell assembly design (Supplementary Fig. 7) following our previous studies^{14,28,79}. Samples were isolated from a graphite heater using an alumina sleeve, which also acted as a thermal insulator to effectively restrict lateral heat flow. Three identically double-side polished disks were piled at the center of a pyrophyllite cubic pressure medium. A K-type (NiCr–NiAl) thermocouple and an impulse heater (Ni or Mo) were set on each interface between two disks. Nickel rods in contact with the samples were used as heat sinks to ensure a constant temperature boundary condition.

In-situ measurements of D and κ were performed at pressures up to 3 GPa and temperatures up to 873 K using the transient plane-source method³⁰. The assembly was compressed to the desired pressure at room temperature, followed by heating to the target temperature over approximately 60 min. The assembly was then cooled at a rate of 10 °C/min, during which the D and κ were measured every 50 or 100 K. More than three repeated measurements at each temperature were performed to check for data reproducibility. The pressure was calibrated using the phase transition of Bi (2.54 GPa at room temperature) and melting of halide (high temperature). The uncertainties of the pressure estimation and temperature measurement with a K-type thermocouple are approximately 0.2 GPa and 1 K, respectively. To avoid any possible dehydration of garnet and omphacite and melting of eclogite, the experiments were performed at temperatures below 873 K.

Data acquisition. The thermal disturbance caused by impulse heating was monitored by the thermocouple under each pressure and temperature condition. The temperature variation (ΔT) at the thermocouple position can be expressed as a function of time (t)^{30,80}:

$$\Delta T = A \sum_{n=1}^{\infty} \frac{1}{n^2} \sin \frac{n\pi}{3} \sin \frac{n\pi d}{h} \exp -n^2 B t [\exp(n^2 B t) - 1] : t > \tau \quad (6)$$

where τ is the duration of impulse heating (s), d is the distance between the impulse heater and thermocouple (m), and h is the total height of the three sample disks (m). The parameters A and B are defined as:

$$A = \frac{2Qh}{\pi^2 \kappa S}, \quad B = \frac{\pi^2 D}{h^2} \quad (7)$$

where Q is the power of the impulse heating (W), S is the area of the impulse heater (m^2), κ is the thermal conductivity ($\text{Wm}^{-1} \text{K}^{-1}$), and D is the thermal diffusivity ($\text{mm}^2 \text{s}^{-1}$).

The temperature-time curve (ΔT - t) was obtained in the experiments, whereas the parameters A and B were determined through the least-square fitting of the ΔT - t curves in Eq. (6) by sweeping n up to 15, whose reliability has been verified by finite element simulations⁸¹. Once A and B are obtained, D and κ can be calculated from Eq. (7).

The errors of the experimental results of D and κ mainly come from the uncertainty of the sample thickness h , heating area S , pulse heating power Q , temperature, and the fitting errors of A and B . The sample geometry during compression and heating was corrected based on the equation of state of eclogite⁸² with the assumption of

isotropic contraction of the eclogite sample. The change of impulse heater area was calculated using the method proposed by Wang et al.²⁰. The temperature disturbance across the sample associated with pulse heating was ~3 K with a 10-W pulse power. The effect of temperature heterogeneity on the measured results was thus negligible. Our previous work²⁹ also demonstrated a negligible influence of sample thickness and heating history (heating or cooling cycles) on the experimental results using the transient plane-source method. The total experimental uncertainties of D and κ originating from the abovementioned factors are therefore expected to be less than 5% (Supplementary Table 1).

As discussed above, the experimentally determined κ (and D) based on the contact method contains the contributions of both κ_{lat} and κ_{rad} . Practically, it is difficult to distinguish them in experiments^{29,75,83}. However, because our experiments were performed under relatively low temperature conditions, the contribution of κ_{rad} is limited. Based on Eq. (4), κ_{rad} is less than 3% of κ_{eff} . Therefore, the contribution of κ_{rad} has negligible effect on κ_{lat} determined in this study.

Simulation of geotherm profiles in the lithosphere

The crust and lithosphere are divided into a finite number of thin layers of thickness Δz for each layer considering steady-state conductive heat transfer in a medium with arbitrary heat production. The heat generation (A) and thermal conductivity (κ) are assumed to be constant in each layer. The temperature profile within each layer is computed by a one-dimensional model using a boot-strapping method^{46,47}:

$$T(z) = T_T + (Q_T/\kappa) \times z - (A/2\kappa) \times z^2 \quad (8)$$

where T_T and Q_T are the temperature and heat flow at the top of the layer, respectively, and z is the depth within the layer.

The temperature and heat flow at the bottom of the layer (T_B and Q_B , respectively) can be calculated from T_T and Q_T :

$$T_B = T_T + (Q_T/\kappa) \times \Delta z - (A/2\kappa) \times \Delta z^2 \quad (9)$$

$$Q_B = Q_T - A \times \Delta z \quad (10)$$

in which T_B and Q_B are set as the T_T and Q_T values for the underlying layer.

By applying Eqs. (8)–(10), the geotherm profiles are calculated from the surface downward using a depth increment of 10 m in each step ($\Delta z = 10$ m). Following this approach, the crustal structures, composition, and heat production in the Sulu UHPM belt^{50,51} and Himalaya-Tibet orogenic belt^{48,49,52,84,85} are shown in Supplementary Fig. 5, and the temperature profiles are given in Fig. 3. The κ of ultrahigh-pressure eclogite, granite, gneiss, amphibolite, and granulite are taken from this study and references^{28,41,42}. Two alternative heat productions were assumed in the lithospheric mantle⁵¹: a depleted mantle with $A = 0.02 \mu\text{W m}^{-3}$; and an enriched mantle with $A = 0.18 \mu\text{W m}^{-3}$. Note that the surface heat flow Q_T exerts the most significant influence on the corrected and uncorrected geotherms in Eq. (5), and consequently on the lithosphere thickness. Q_T is 65 mW m^{-2} for the Sulu belt and 75 mW m^{-2} for the Tibetan Plateau based on the database of surface heat flow^{44,45}. The mantle adiabat was set to a potential temperature of 1573 K with a gradient of 0.3 K/km, and the surface temperature was fixed at 283 K.

Data availability

The data that support the findings of this study are available from the corresponding authors upon request.

References

- Jamveit, B., Ben-Zion, Y., Renard, F. & Austrheim, H. Earthquake-induced transformation of the lower crust. *Nature* **556**, 487–491 (2018).
- Kind, R. et al. Evidence from earthquake data for a partially molten crustal layer in southern Tibet. *Science* **274**, 1692–1694 (1996).
- Nábělek, J. et al. Underplating in the Himalaya-Tibet collision zone revealed by the Hi-CLIMB experiment. *Science* **325**, 1371–1374 (2009).
- Yang, W. C. The crust and upper mantle of the Sulu UHPM belt. *Tectonophysics* **475**, 226–234 (2009).
- Nelson, K. D. et al. Partially molten middle crust beneath southern Tibet: Synthesis of project INDEPTH results. *Science* **274**, 1684–1688 (1996).
- Wei, W. et al. Detection of widespread fluids in the Tibetan crust by magnetotelluric studies. *Science* **292**, 716–719 (2001).
- Unsworth, M. J. et al. Crustal rheology of the Himalaya and Southern Tibet inferred from magnetotelluric data. *Nature* **438**, 78–81 (2005).
- Xiao, Q. et al. Deep electrical structure of the Sulu orogen and neighboring areas. *Sci. China Ser. D: Earth Sci.* **52**, 420–430 (2009).
- Bai, D. et al. Crustal deformation of the eastern Tibetan plateau revealed by magnetotelluric imaging. *Nat. Geosci.* **3**, 358–362 (2010).
- Liu, H., Zhu, Q. & Yang, X. Electrical conductivity of OH-bearing omphacite and garnet in eclogite: the quantitative dependence on water content. *Contrib. Mineral. Petrol.* **176**, 57 (2019).
- Zheng, Y. F., Xia, Q. X., Chen, R. X. & Gao, X. Y. Partial melting, fluid supercriticality and element mobility in ultrahigh-pressure metamorphic rocks during continental collision. *Earth-Sci. Rev.* **107**, 342–374 (2011).
- Austrheim, H. & Boundy, T. M. Pseudotachylytes generated during seismic faulting and eclogitization of the deep crust. *Science* **265**, 82–83 (1994).
- Krystopowicz, N. J. & Currie, C. A. Crustal eclogitization and lithosphere delamination in orogens. *Earth Planet. Sci. Lett.* **361**, 195–207 (2013).
- Zhang, B. H., Zhao, C. C., Ge, J. H. & Yoshino, T. Electrical conductivity of omphacite as a function of water content and implications for high conductivity anomalies in the Dabie-Sulu UHPM belts and Tibet. *J. Geophys. Res.* **124**, 12523–12536 (2019).
- Chantel, J. et al. Experimental evidence supports mantle partial melting in the asthenosphere. *Sci. Adv.* **2**, e1600246 (2016).
- Yoshino, T., Laumonier, M., McIsaac, E. & Katsura, T. Electrical conductivity of basaltic and carbonate melt-bearing peridotites at high pressures: implications for melt distribution and melt fraction in the upper mantle. *Earth Planet. Sci. Lett.* **295**, 593–602 (2010).
- Zhang, B. H., Yoshino, T., Yamazaki, D., Manthilake, G. & Katsura, T. Electrical conductivity anisotropy of partially molten peridotite under shear deformation. *Earth Planet. Sci. Lett.* **405**, 98–109 (2014).
- Zhang, B. H., Guo, X., Yoshino, T. & Xia, Q. K. Electrical conductivity of melts: Implications for conductivity anomalies in the Earth's mantle. *Nat. Sci. Rev.* **8**, nwab064 (2021).
- Dobson, D. P. et al. Thermal diffusivity of MORB-composition rocks to 15 GPa: Implications for triggering of deep seismicity. *High Press. Res.* **30**, 406–414 (2010).
- Wang, C. et al. Measurement of thermal conductivity of omphacite, jadeite, and diopside up to 14 GPa and 1000 K: Implication for the role of eclogite in subduction slab. *J. Geophys. Res.* **119**, 6277–6287 (2014).
- Zheng, Y. F. Metamorphic chemical geodynamics in continental subduction zones. *Chem. Geol.* **328**, 5–48 (2012).
- Hermann, J., Zheng, Y. F. & Rubatto, D. Deep fluids in subducted continental crust. *Elements* **9**, 281–287 (2013).

23. Zheng, Y. F., Chen, R. X., Xu, Z. & Zhang, S. The transport of water in subduction zones. *Sci. China Earth Sci.* **59**, 651–682 (2016).
24. Chang, Y. Y., Hsieh, W. P., Tan, E. & Chen, J. Hydration-reduced lattice thermal conductivity of olivine in Earth's upper mantle. *Proc. Natl. Acad. Sci. USA* **114**, 4078–4081 (2017).
25. Zhang, B. H., Ge, J. H., Xiong, Z. L. & Zhai, S. M. Effect of water on the thermal properties of olivine with implications for lunar internal temperature. *J. Geophys. Res.* **124**, 3469–3481 (2019).
26. Xu, Y. S. et al. Thermal diffusivity and conductivity of olivine, wadsleyite and ringwoodite to 20 GPa and 1373 K. *Phys. Earth Planet. Inter.* **143**, 321–336 (2004).
27. Ray, L., Förster, H. J., Schilling, F. R. & Förster, A. Thermal diffusivity of felsic to mafic granulites at elevated temperatures. *Earth Planet. Sci. Lett.* **251**, 241–253 (2006).
28. Fu, H. F. et al. Thermal diffusivity and thermal conductivity of granulites at 283–988 K and 0.3–1.5 GPa. *Am. Mineral.* **104**, 1533–1545 (2019).
29. Hofmeister, A. M. Pressure dependence of thermal transport properties. *Proc. Natl. Acad. Sci. USA* **104**, 9192–9197 (2007).
30. Osako, M., Ito, E. & Yoneda, A. Simultaneous measurements of thermal conductivity and thermal diffusivity for garnet and olivine under high pressure. *Phys. Earth Planet. Inter.* **143**, 311–320 (2004).
31. Koch-Müller, M., Matsyuk, S. S. & Wirth, R. Hydroxyl in omphacites and omphacitic clinopyroxenes of upper mantle to lower crustal origin beneath the Siberian platform. *Am. Mineral.* **89**, 921–931 (2004).
32. Katayama, I., Nakashima, S. & Yurimoto, H. Water content in natural eclogite and implication for water transport into the deep upper mantle. *Lithos* **86**, 245–259 (2006).
33. Manthilake, G. M., de Koker, N., Frost, D. J. & McCammon, C. A. Lattice thermal conductivity of lower mantle minerals and heat flux from Earth's core. *Proc. Natl. Acad. Sci. USA* **108**, 17901–17904 (2011).
34. Zheng, Y. F., Xia, Q. X., Chen, R. X. & Gao, X. Y. Partial melting, fluid supercriticality and element mobility in ultrahigh-pressure metamorphic rocks during continental collision. *Earth-Sci. Rev.* **107**, 342–374 (2011).
35. Sawyer, E. W., Cesare, B. & Brown, M. When the continental crust melts. *Elements* **7**, 229–234 (2011).
36. Xu, H. J., Ye, K. & Zhang, J. F. Prograde metamorphism, decompressional partial melting and subsequent melt crystallization and segregation in the Weihai migmatitic gneisses, Sulu UHP terrane, Eastern China. *Chem. Geol.* **341**, 16–37 (2013).
37. Zeng, L. S., Liang, F. H., Asimow, P., Chen, F. Y. & Chen, J. Partial melting of deeply subducted continental crust and the formation of quartzo-feldspathic polyphase inclusions in the Sulu UHP eclogites. *Chin. Sci. Bull.* **54**, 2580–2594 (2009).
38. Kohn, M. J. Himalayan metamorphism and its tectonic implications. *Annu. Rev. Earth Planet. Sci.* **42**, 381–419 (2014).
39. Wang, L. et al. Partial melting of deeply subducted eclogite from the Sulu orogen in China. *Nat. Commun.* **5**, 5604 (2014).
40. Li, W. C., Chen, R. X., Zheng, Y. F., Tang, H. & Hu, Z. Two episodes of partial melting in ultrahigh-pressure migmatites from deeply subducted continental crust in the Sulu orogen, China. *GSA Bull.* **128**, 1521–1542 (2016).
41. Seipold, U. & Huenges, E. Thermal properties of gneisses and amphibolites—high pressure and high temperature investigations of KTB-rock samples. *Tectonophysics* **291**, 173–178 (1998).
42. Merriman, J. D., Whittington, A. G., Hofmeister, A. M., Nabelek, P. I. & Benn, K. Thermal transport properties of major Archean rock types to high temperature and implications for cratonic geotherms. *Pre-cam. Res.* **233**, 358–372 (2013).
43. Xia, Q. K. et al. Water in the upper mantle and deep crust of eastern China: concentration, distribution and implications. *Nat. Sci. Rev.* **6**, 125–144 (2009).
44. The official database of the international heat flow commission (www.ihfc-iugg.org).
45. Lucazeau, F. Analysis and mapping of an updated terrestrial heat flow data set. *Geochem. Geophys. Geosyst.* **20**, 4001–4024 (2019).
46. Hasterok, D. & Chapman, D. S. Heat production and geotherms for the continental lithosphere. *Earth Planet. Sci. Lett.* **307**, 59–70 (2011).
47. Furlong, K. P. & Chapman, D. S. Heat flow, heat generation, and the thermal state of the lithosphere. *Annu. Rev. Earth Planet. Sci.* **41**, 385–410 (2013).
48. Owens, T. J. & Zandt, G. Implications of crustal property variations for models of Tibetan plateau evolution. *Nature* **387**, 37–43 (1997).
49. Li, W. et al. Petrofabrics and seismic properties of Himalayan amphibolites: Implications for a thick anisotropic deep crust beneath southern Tibet. *J. Geophys. Res.* **125**, e2019JB018700 (2020).
50. Chi, Q. H. & Yan, M. C. Radioactive elements of rocks in North China Platform and the thermal structure and temperature distribution of the modern continental lithosphere. *Chin. J. Geophys.* **41**, 38–48 (1998).
51. He, L., Hu, S., Yang, W. & Wang, J. Radiogenic heat production in the lithosphere of Sulu ultrahigh-pressure metamorphic belt. *Earth Planet. Sci. Lett.* **277**, 525–538 (2009).
52. Goes, S., Hasterok, D., Schutt, D. L. & Klöcking, M. Continental lithospheric temperatures: a review. *Phys. Earth Planet. Inter.* **306**, 106509 (2020).
53. Hermann, J. Experimental constraints on phase relations in subducted continental crust. *Contrib. Mineral. Petrol.* **143**, 219–235 (2002).
54. Holtz, F., Becker, A. & Wilhelm, J. The water-undersaturated and dry Qz-Ab-Or system revisited: Experimental results at very low water activities and geological implications. *Contrib. Mineral. Petrol.* **141**, 347–357 (2001).
55. Gilotti, J. A. The realm of ultrahigh-pressure metamorphism. *Elements* **9**, 255–260 (2013).
56. Annen, C., Blundy, J. D. & Sparks, R. S. J. The genesis of intermediate and silicic magmas in deep crustal hot zones. *J. Petrol.* **47**, 505–539 (2006).
57. Zheng, Y. F., Chen, R. X. & Zhao, Z. F. Chemical geodynamics of continental subduction-zone metamorphism: Insights from studies of the Chinese Continental Scientific Drilling (CCSD) core samples. *Tectonophysics* **475**, 327–358 (2009).
58. Zhang, R. Y., Liou, J. G. & Ernst, W. G. The Dabie–Sulu continental collision zone: a comprehensive review. *Gondwana Res.* **16**, 1–26 (2009).
59. Liu, F. L. & Liou, J. G. Zircon as the best mineral for P–T–time history of UHP metamorphism: a review on mineral inclusions and U–Pb SHRIMP ages of zircons from the Dabie–Sulu UHP rocks. *J. Asian Earth Sci.* **40**, 1–39 (2011).
60. McClelland, W. C. & Lapen, T. J. Linking time to the pressure–temperature path for ultrahigh-pressure rocks. *Elements* **9**, 273–279 (2013).
61. Wallis, S. et al. Role of partial melting in the evolution of the Sulu (eastern China) ultrahigh-pressure terrane. *Geology* **33**, 129–132 (2005).
62. Hermann, J., Spandler, C., Hack, A. & Korsakov, A. V. Aqueous fluids and hydrous melts in high-pressure and ultrahigh-pressure rocks: Implications for element transfer in subduction zones. *Lithos* **92**, 399–417 (2006).
63. Kouketsu, Y., Hattori, K., Guillot, S. & Rayner, N. Eocene to Oligocene retrogression and recrystallization of the Stak eclogite in northwest Himalaya. *Lithos* **240**, 155–166 (2016).
64. Wang, J. M. et al. First evidence of eclogites overprinted by ultrahigh temperature metamorphism in Everest East, Himalaya:

- Implications for collisional tectonics on early Earth. *Earth Planet. Sci. Lett.* **558**, 116760 (2021).
65. Renner, J., Evans, B. & Hirth, G. On the rheologically critical melt fraction. *Earth Planet. Sci. Lett.* **181**, 585–594 (2000).
 66. Rosenberg, C. L. & Handy, M. R. Experimental deformation of partially melted granite revisited: Implications for the continental crust. *J. Metamor. Geol.* **23**, 19–28 (2005).
 67. Labrousse, L., Prouteau, G. & Ganzhorn, A. C. Continental exhumation triggered by partial melting at ultrahigh pressure. *Geology* **39**, 1171–1174 (2014).
 68. Ernst, W. G., Zhou, G., Liou, J. G., Eide, E. & Wang, X. High-pressure and superhigh-pressure metamorphic terranes in the Qinling-Dabie mountain belt, central China: Early- to mid-Phanerozoic accretion of the western paleo-Pacific Rim. *Pac. Sci. Assoc. Inform. Bull.* **43**, 6–15 (1991).
 69. Zheng, Y. F., Fu, B., Gong, B. & Li, L. Stable isotope geochemistry of ultrahigh pressure metamorphic rocks from the Dabie–Sulu orogen in China: Implications for geodynamics and fluid regime. *Earth-Sci. Rev.* **62**, 105–161 (2003).
 70. Zheng, Y. F. A perspective view on ultrahigh-pressure metamorphism and continental collision in the Dabie–Sulu orogenic belt. *Chin. Sci. Bull.* **53**, 3081–3104 (2008).
 71. Tang, H. F., Liu, C. Q., Nakai, S. I. & Orihashi, Y. Geochemistry of eclogites from the Dabie–Sulu terrane, eastern China: New insights into protoliths and trace element behaviour during UHP metamorphism. *Lithos* **95**, 441–457 (2007).
 72. Zhang, R. Y., Liou, J. G., Zheng, Y. F. & Fu, B. Transition of UHP eclogites to gneissic rocks of low-grade amphibolite facies during exhumation: Evidence from the Dabie terrane, central China. *Lithos* **70**, 269–291 (2003).
 73. Bell, D. R., Ihinger, P. D. & Rossman, G. R. Quantitative analysis of hydroxyl in garnet and pyroxene. *Am. Mineral.* **80**, 465–474 (1995).
 74. Paterson, M. S. The determination of hydroxyl by infrared absorption in quartz, silicate glasses and similar materials. *Bull. Mineral.* **105**, 20–29 (1982).
 75. Hofmeister, A. M. Mantle values of thermal conductivity and the geotherm from phonon lifetimes. *Science* **283**, 1699–1705 (1999).
 76. Anderson, O. L. & Isaak, D. G. Elastic constants of mantle minerals at high temperature. *Mineral Phys. Crystallogr.: A Handbook Phys. Constants* **2**, 64–97 (1995).
 77. Hao, M., Zhang, J. S., Zhou, W. Y. & Wang, Q. Seismic visibility of eclogite in the Earth's upper mantle: Implications from high pressure-temperature single-crystal elastic properties of omphacite. *J. Geophys. Res.* **126**, e2021JB021683 (2021).
 78. Hofmeister, A. M., Branlund, J. M. & Pertermann, M. Properties of rocks and minerals—Thermal conductivity of the Earth. *Treatise Geophys.* **2**, 543–577 (2007).
 79. Xiong, Z. L., Zhang, B. H., Ge, J. H., Zhai, S. M. & Guo, X. Z. Thermal diffusivity and thermal conductivity of alkali feldspar at 0.8–3 GPa and 300–873 K. *Contrib. Mineral. Petrol.* **176**, 42 (2021).
 80. Dzhavadov, L. N. Measurement of thermophysical properties of dielectrics under pressure. *High Temp. High Press.* **7**, 49–54 (1975).
 81. Yoneda, A., Osako, M. & Ito, E. Heat capacity measurement under high pressure: a finite element method assessment. *Phys. Earth Planet. Inter.* **174**, 309–314 (2009).
 82. Xu, J. et al. Thermoelastic properties of eclogitic garnets and omphacites: Implications for deep subduction of oceanic crust and density anomalies in the upper mantle. *Geophys. Res. Lett.* **46**, 179–188 (2019).
 83. Förster, A., Fuchs, S., Förster, H. J. & Norden, B. Ambiguity of crustal geotherms: a thermal-conductivity perspective. *Geothermics* **89**, 101937 (2021).
 84. Hacker, B. R. et al. Hot and dry deep crustal xenoliths from Tibet. *Science* **287**, 2463–2466 (2000).
 85. Wang, C. Y., Chen, W. P. & Wang, L. P. Temperature beneath Tibet. *Earth Planet. Sci. Lett.* **375**, 326–337 (2013).

Acknowledgements

We appreciate the help of Dr. Hongfeng Tang for thin section identification, Dr. Xiaozhi Yang for FTIR measurements and Drs. Jia Liu, Xiaoyan Gu, Yantao Hao, and Wancai Li for helpful discussions. This study was financially supported by the Basic Science Center Program for Multi-phase Media Evolution in Hypergravity of the National Natural Science Foundation of China (51988101), the National Natural Science Foundation of China (41973056, 41773056) to B.H.Z., the Fundamental Research Funds for the Central Universities (K20210168) to Q.K.X., and Key Research Program of Frontier Sciences of CAS (ZDBS-LY-DQC015) to B.H.Z.

Author contributions

B.H.Z. conceived the idea and designed the experiments. B.H.Z. and H.Z.F. wrote the paper. J.H.G. performed the experiments. B.H.Z. and J.H.G. analyzed the data. L.S.Z. and Q.K.X. contributed to the data interpretation. All authors participated in the discussion and agreed on the content.

Competing interests

The authors declare no competing interests.

Additional information

Supplementary information The online version contains

supplementary material available at <https://doi.org/10.1038/s41467-022-32484-w>.

Correspondence and requests for materials should be addressed to Baohua Zhang or Qunke Xia.

Peer review information *Nature Communications* thanks Aphrodite Indares and the other, anonymous, reviewer(s) for their contribution to the peer review of this work. Peer reviewer reports are available.

Reprints and permission information is available at <http://www.nature.com/reprints>

Publisher's note Springer Nature remains neutral with regard to jurisdictional claims in published maps and institutional affiliations.

Open Access This article is licensed under a Creative Commons Attribution 4.0 International License, which permits use, sharing, adaptation, distribution and reproduction in any medium or format, as long as you give appropriate credit to the original author(s) and the source, provide a link to the Creative Commons license, and indicate if changes were made. The images or other third party material in this article are included in the article's Creative Commons license, unless indicated otherwise in a credit line to the material. If material is not included in the article's Creative Commons license and your intended use is not permitted by statutory regulation or exceeds the permitted use, you will need to obtain permission directly from the copyright holder. To view a copy of this license, visit <http://creativecommons.org/licenses/by/4.0/>.

© The Author(s) 2022